Asymmetrical morphological evolution and energy conversion of droplets impacting on the moving film

Article

Published Version

It is advisable to refer to the publisher's version if you intend to cite from the work. See Guidance on citing.

To link to this article DOI: http://dx.doi.org/10.1063/5.0244521

www.reading.ac.uk/centaur

CentAUR

Central Archive at the University of Reading

Reading's research outputs online

Asymmetrical morphological evolution and energy conversion of droplets impacting on the moving film

Hongbing Ding (丁红兵) ⓘ ; Xutian Chai (柴旭天); Xinyu Song (宋鑫宇); Yan Yang ✉ ; Chuang Wen ✉ ⓘ

Check for updates

View Online

Export Citation

Articles You May Be Interested In

06 March 2025 14:54:52

Asymmetrical morphological evolution and energy conversion of droplets impacting on the moving film

View Online　　Export Citation　　CrossMark

Hongbing Ding (丁红兵),[1] (iD) Xutian Chai (柴旭天),[1] Xinyu Song (宋鑫宇),[1] Yan Yang,[2,a] and Chuang Wen[3,a] (iD)

AFFILIATIONS

[1]Tianjin Key Laboratory of Process Measurement and Control, School of Electrical and Information Engineering, Tianjin University, Tianjin 300072, China

[2]Faculty of Environment, Science and Economy, University of Exeter, Exeter EX4 4QF, United Kingdom

[3]School of the Built Environment, University of Reading, Reading RG6 6AH, United Kingdom

[a]Authors to whom correspondence should be addressed: y.yang7@exeter.ac.uk and c.wen@reading.ac.uk

ABSTRACT

Droplet impacting on the film has been an important research topic, which is relevant to many important industries and is of high utilization value. The droplet impacting process shows excellent mass and heat transfer capability, whereas the liquid film is often in a flowing state, the morphological deformation and energy conversion of successive droplets impacting a moving liquid film were investigated. A three-dimensional volume of fluid model coupled with level-set function was established to investigate the single and successive droplet impact on the moving film. The asymmetry dynamic and energy dissipation and in the morphological evolution of the simultaneous single and successive droplet impacting processes under different droplet Weber numbers We_d and film Reynolds numbers Re_f were thoroughly investigated. With smaller We_d and larger Re_f, the liquid sheet downstream of the crown is more suppressed and the asymmetry of the crown is more significant. When Re_f is constant, the dimensionless radius of the crown is related to the $We_d^{0.2}$ and also to the power of dimensionless time, with the exponents differing between the upstream and downstream. The relationship of energy dissipation with dimensionless number was discussed, in which the kinetic energy E_k reduction accounts for a major part of the dissipation even though the surface energy E_s increases due to the formation of the crown. Additionally, the upstream liquid sheets merging of the inner and outer crowns due to successive droplets continuous impacting on the moving film were also observed. With larger Re_f and lower impingement frequency, the merging of the upstream liquid sheets is earlier.

NOMENCLATURE

A_{G-L}	Gas–liquid interface area (m^2)
d_{eq}	Equivalent diameter (mm)
d_h	Horizontal diameter of droplet (mm)
d_s	Droplet spreading distance (mm)
d_s^*	Dimensionless droplet spreading distance ($= \frac{d_s}{d_0}$)
d_v	Vertical diameter of droplet (mm)
d_0	Droplet diameter (mm)
E_k	Kinetic energy (J)
E_p	Potential energy (J)
E_s	Surface energy (J)
E_{total}	Sum of E_s, E_k, and E_p (J)
E_0	Initial energy of droplet
f	Frequency of successive droplets (Hz)
h_f	Film thickness (mm)
Q_p	Flow rate of the pump which drive the liquid film
Q_s	Flow rate of the syringe pump (ml/min)
Re_d	Droplet Reynolds number ($= \frac{\rho v_0 d_0}{\mu}$)
Re_f	Film Reynolds number ($= \frac{\rho v_f h_f}{\mu}$)
R_d	Crown spreading distance downstream (mm)
R_d^*	Dimensionless crown spreading distance downstream ($= \frac{R_d}{d_0}$)
R_u	Crown spreading distance upstream (mm)
R_u^*	Dimensionless crown spreading distance upstream ($= \frac{R_u}{d_0}$)
$t*$	Dimensionless time ($= \frac{t * v_0}{d_0}$)

06 March 2025 14:54:52

t_d^*	Dimensionless time of successive droplets impact ($= tf$)
v_0	Droplet velocity (m/s)
v_f	Film velocity (m/s)
W	Energy dissipation (J)
We_d	Droplet Weber number ($= \frac{\rho v_0^2 d_0}{\sigma}$)
α	Volume fraction
θ	Wall inclined angle
μ	Dynamic viscosity (Pa s)
ρ	Density (kg/m^3)
σ	Surface tension (mN/m)
φ	Level set function

I. INTRODUCTION

The ubiquitous phenomenon of droplet impacting on dry and wetted walls is of natural and industrial significance.[1] It is widely present in air treatment equipment, public space cooling, inkjet printing, fuel atomization, and other fields.[2–5] Much numerical and experimental investigations have been conducted on the droplet impacting process comprising rich aspects of fluid mechanics and thermodynamics,[6,7] such as complex multiphase flow regimes, interactions between surface tension and inertial forces, etc., deformation of interface, splash threshold, heat transfer, and energy consumption. However, when droplets impact moving liquid films, the topological changes and energy transformations become more complex, necessitating further analysis. The morphological evolution and heat transfer characteristics of multiple impacting droplets are crucial due to their broad applications.

Typically, the primary numerical methods used to study droplet impact on films or pools are the volume of fluid (VOF) method and the level-set method.[8,9] Some researchers have also utilized the lattice Boltzmann method (LBM).[10,11] The VOF method coupled with the level-set method (CLSVOF) plays a crucial role in tracking two-phase flow interfaces.[12] The droplet impact process can be classified based on the impacted surface into dry walls and liquids. For droplets impacting liquids, studies often focus on static thin liquid films, moving thin liquid films, and liquid pools. In the case of droplets impacting dry walls, the primary focus has been on the dynamics of spreading and splashing,[13,14] with particular attention given to the effects of different liquids[15,16] and surface properties, especially superhydrophobic surfaces.[17–19] Furthermore, the changes in heat transfer caused by droplet impact on hot walls have also been a significant area of research. Research on droplet impact on stationary thin liquid films has primarily focused on the formation and breakup of crowns. Worthington[20] captured the crown formed when water droplets splashed into milk, and subsequent studies have explored the morphology and evolution of these crowns. Vander Wal et al.[21] experimentally discussed the impact process, considering dimensionless film thicknesses between 0.1 and 10, and demonstrated that secondary droplet formation increases with surface tension and viscosity for both prompt and delayed splashes. Liang et al.[22] highlighted that crown height and secondary droplet generation cannot be accurately simulated in two-dimensional models. In addition to horizontal walls, studies have also explored droplet impacts on spherical targets, with Bakshi et al.[23] proposing three distinct phases: initial drop deformation, inertia-dominated phase, and viscosity-dominated phase. Muthusamy et al.[24] found that the droplet Weber number significantly affects spread-splash transitions and the effectiveness of film heat transfer, with

intense splashing reducing effective cooling area. In practical applications, the presence of tangential relative velocities between droplets and films adds complexity. Studies on oblique droplets impacting stationary films and vertical droplets impacting flowing surface have gained attention. Velocity difference between the droplet and moving film causes the crown upstream to break more easily, resulting in asymmetry between the crowns at the upstream and downstream.[23,25] Stober et al.[26] studied oblique droplets impacting a stationary horizontal film, where adjustments to impact velocity and angle influenced the dynamics of oblique impacts. Chen et al.[27] used a three-dimensional multiphase solver to examine droplet impacts at different angles, finding that decreasing the impact angle increased the splashing of minor droplets. Other studies[28,29] observed that higher impact angles suppressed secondary droplet production. Ray et al.[30] showed that angles above 60° reduced secondary droplet formation, while a higher Weber number led to more momentum transfer and more secondary droplets. Cao et al.[31] explored oblique droplet impacts on films, revealing that increased tangential velocity enhanced crown evolution. Furthermore, Li et al.[32] found that surface shear force significantly influences droplet dynamics, affecting spreading, stretching, and wake flow, which contributes to a deeper understanding of droplet behavior and lays the groundwork for further research.

The impacted film is often in motion, especially during processes like spray cooling, where liquid falling onto a hot surface accumulates and flows away, causing subsequent droplets to impact the moving film. This dynamic interaction intensifies the interactions between the droplets, film, and surface, leading to more complex deformation of the gas–liquid interface. Consequently, studying droplet impact on moving films is crucial. This effect resembles the asymmetry observed when oblique droplets impact a stationary film.[33,34] Gao and Li[35] investigated the impact of a single droplet on a flowing film, focusing on drop spreading, crown sheet stretching in the rising direction, and predicting splashing occurrence. Zhao et al.[36] numerically studied droplet impact on a moving film and found that as film thickness increased, both the volume of liquid entering the crown and the angle between the crown wall and film expanded. Wu et al.[37] examined the interaction between oblique droplets and a moving film, finding that when the horizontal velocity of the droplet was lower than that of the film, crown height, pressure difference, and secondary droplet count were greater upstream. The opposite occurred when the horizontal velocity of the droplet exceeded that of the film. Che et al.[38] employed high-speed imaging to investigate droplet impacts on inclined falling liquid films, identifying phenomena such as bouncing and coalescence. Their results showed that the liquid film flow rate significantly influences droplet behavior, leading to more complex impact processes compared to static films. They also provided a zoning diagram based on the liquid film Reynolds number and droplet Weber number. Similarly, Shan et al.[39] numerically and experimentally studied interface changes under different droplet and film velocities, demonstrating that the relationship between splashing, droplet Weber number, and film Reynolds number could predict splashing behavior. Liang et al.[40] examined droplet impact on a flowing liquid film and found a linear relationship between the Weber and Reynolds numbers, which defines the splashing threshold. Higher flow rates caused asymmetric interfacial evolution, with splashing occurring upstream and suppressed downstream, while impact velocity increased crown height, particularly upstream. The evolution of the liquid crown during droplet

06 March 2025 14:54:52

impact is influenced by multiple factors. Rioboo et al.[41] experimentally investigated the impact of liquid drops on solid, dry surfaces, focusing on the effects of various parameters, and highlighted that the dimensionless spreading factor of droplets is a complex function of the Weber number, Reynolds number, dimensionless time, and contact angle. Khan et al.,[42] investigated the impact dynamics of non-spherical droplets on a thin water film, revealing that droplet shape significantly influences splashing and crown formation. Oblate droplets were more prone to splashing, while prolate droplets exhibited greater splash resistance. Wang et al.[43] examined the impact dynamics of low-viscosity nanodroplets on surfaces with contact angles ranging from $\theta = 73°$ to $180°$, deriving scaling laws for the maximum spreading factor and the dimensionless numbers, such as Reynolds and Weber numbers.

As mentioned above, existing research primarily focuses on the morphological evolution of droplets, interface changes, and the quantitative description of splash behavior,[38–40] while the energy transfer and transformation during droplet impact, particularly the interactions between kinetic energy, surface tension energy, and potential energy, remain underexplored. In addition, the scaling laws governing the morphological evolution between droplets and flowing liquid films are complex[41–43] and deserve further attention, as do the interactions between different droplets. Further investigation into the energy transformations and couplings during droplet impact would provide a deeper theoretical foundation for understanding droplet behavior under various conditions and contribute to optimizing related engineering applications.

A model of multiple droplets impacting the moving film based on CLSVOF was developed to investigate the morphological evolution and the energy variation. The experimental data were derived by the setup introduced in Sec. II. The model was validated to achieve droplet train impacting on the inclined wall and the moving film in Sec. III. In Sec. IV, the influences of We_d and Re_f on the crown morphology and energy evolution during single droplet impacting on the moving film were discussed to contribute to the further utilization of droplet impacting. Finally, velocity distribution and characteristics of both the

inner and outer crowns induced by the successive droplets impacting a moving film was studied further.

II. EXPERIMENT SETUP

The liquid (water, $\mu = 1.01 \times 10^{-3}$ Pa s, $\rho = 996.5$ kg/m^3, and $\sigma = 0.0728$ N/m) pumped from the tank to the reservoir passes through a regulating valve and a rectifier tube and form a moving liquid film on the substrate as shown in Fig. 1. The monodisperse droplets were generated by the droplet generator, which was driven by the amplified frequency signal. Images of the impact were captured by the high-speed camera (Photron FASTCAM Mini UX) with a macro lens (Nikon, 105 mm, f 2.8) and then imaged on the computer at 8000 fps. Diameters d_0 (1.624 mm ± 0.58%–2.087 mm ± 2.02%) and frequency f of droplets were varied by inner diameter of the droplet generator nozzle, the flow rate Q_s of the syringe pump (LEADFLUID TYD02-01, flow rate ranges from 0.1 to 100 ml/min with the maximum relative of ±2%), and the signal frequency. Droplet velocity v_0 at impact can be altered by adjusting the height of the droplet generator of the substrate. The film velocity v_f was determined by averaging the center of gravity displacements of the tracer particle over two adjacent frames of the image. The film thickness h_f at the impact point was calculated by the following equation:

$$h_f = \frac{Q_p}{2\pi x v_f}, \tag{1}$$

where Q_p is the flow rate of liquid film driven by the pump and x is the horizontal distance to the liquid film injection location. The film thickness h_f would remain relatively constant because the ratio of x (12 mm in this paper) to the radius of the liquid column out of the rectifier tube (2 mm in this paper) is much larger than 1.[44]

Taking the moment when the droplet first contacts the film as 0 ms, morphology of a droplet ($d_0 = 2.4203$ mm) impacting the flowing film evolves over time as shown in Fig. 2. Initially, the droplet impacts the film quickly due to the influence of inertial force, and then small jets forming a crown appears. When $t = 1$ ms, the crown has already shown obvious asymmetry, but the crown has not yet broken. Subsequently, the crown gradually expands with time and the
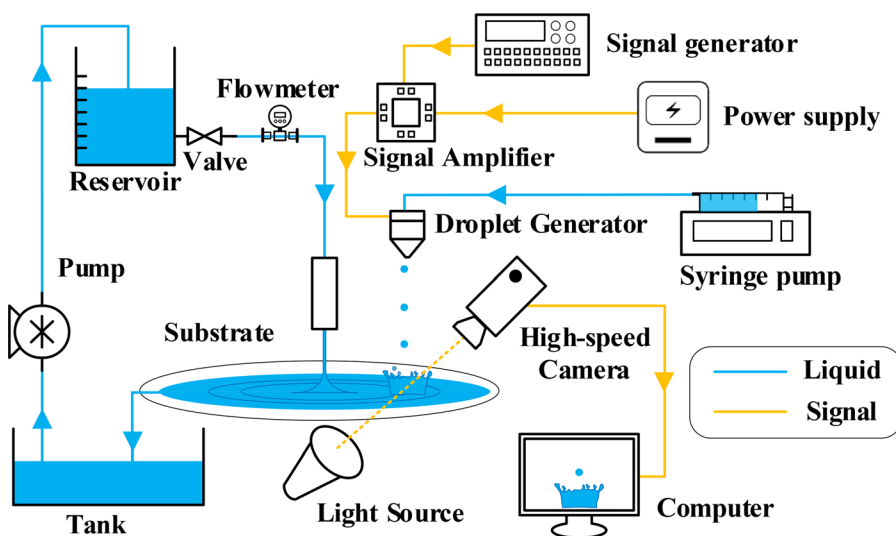
FIG. 1. Experimental setup for continuous monodisperse droplets impacting on the moving film.
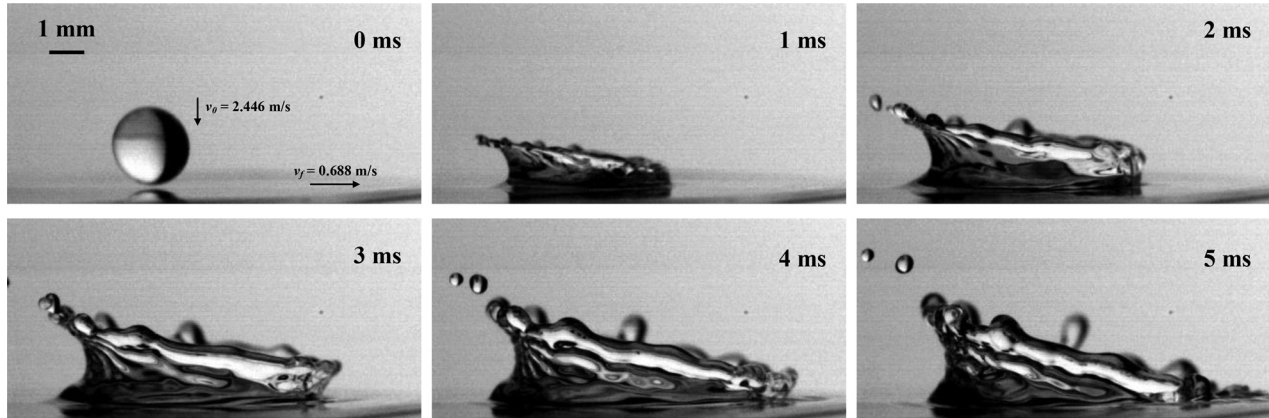
FIG. 2. Morphology evolution when $We_d = 198.187$ and $Re_f = 213.823$.

secondary droplets appear. The crown downstream rose first and then gradually fell, which also reflects the dissipation of liquid kinetic energy until it gradually merged with the moving film at $t = 5$ ms.

Parameter acquisition of experimental results was realized by image recognition. The upstream and downstream spreading radii R_u and R_d of the crown were defined in Fig. 3(a). The equivalent diameter of droplet d_{eq} was calculated from Eq. (2). Droplet velocity v_d was calculated by averaging the center of gravity displacement of the droplet between two frames ΔS_v as Eq. (3),

$$d_{eq} = \left(d_h^2 d_v\right)^{\frac{1}{3}}, \tag{2}$$

where d_h and d_v are horizontal and vertical length, respectively, as shown in Fig. 3(b).

$$v_d = \frac{\Delta S_v}{\Delta t}. \tag{3}$$

III. NUMERICAL MODEL

A 3D model was built to simulate the droplet impact. The volume-of-fluid (VOF) model coupled with level set (CLSVOF)[45] was widely used in two-phase flow to obtain the gas–liquid interface. CLSVOF can solve both the mass non-conservation and the inaccurate calculation of section curvature $\vec{\kappa}$.

A. Governing equations and computational domain

The phase volume fraction α is used in calculating the fluid properties, a volume-averaged values. For instance, ρ was obtained by the following equation:

$$\rho = \alpha_L \rho_L + (1 - \alpha_L)\rho_G, \tag{4}$$

where α_L was calculated as the following equation:

$$\alpha_G = 1 - \alpha_L. \tag{5}$$

Mass and momentum governing equations were shown as the following equations:

$$\frac{\partial}{\partial t}\left(\alpha_q \rho_q\right) + \nabla \cdot \left(\alpha_q \rho_q \vec{u}\right) = 0, \tag{6}$$

$$\frac{\partial}{\partial t}\left(\rho \vec{u}\right) + \nabla \cdot \left(\rho \vec{u}\vec{u}\right) = -\nabla p + \left[\mu\left(\nabla \vec{u} + \nabla \vec{u}^T\right)\right] + \rho \vec{g} + f_{vol}, \tag{7}$$

where $\vec{g}$ and f_{vol} denote the gravitational acceleration and the source term accounting for surface tension, respectively, as described by Brackbill's continuum surface force (CSF) model.[46] The level set function (LSF) φ is defined as a signed distance function to the interface, expressed as
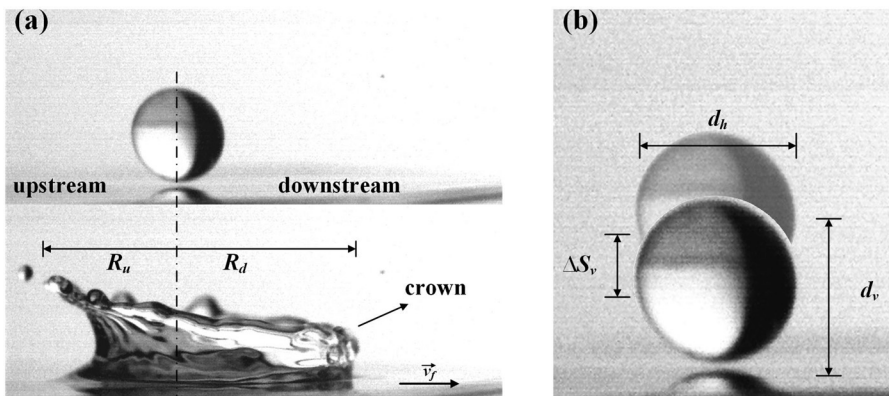

FIG. 3. Definition of crown parameters and the droplet velocity calculation appeared in the study: (a) crown spreading distance upstream and downstream and (b) droplet parameters.

$$\frac{\partial \varphi}{\partial t} + \nabla \cdot (\vec{u_q} \varphi) = 0, \tag{8}$$

where φ equals zero on the interface, and the distance function $\varphi(x, t)$ is calculated as

$$\varphi(x, t) = \begin{cases} +|d|, & \text{primary phase,} \\ 0, & \text{interface,} \\ -|d|, & \text{secondary phase,} \end{cases} \tag{9}$$

where for each x, d is the distance to the interface. The normal $\vec{n}$ and curvature $\vec{\kappa}$ when $\varphi(x, t) = 0$ are obtained by the following equations:[47]

$$\vec{n} = \left. \frac{\nabla \varphi}{|\nabla \varphi|} \right|_{\varphi=0}, \tag{10}$$

$$\vec{\kappa} = \nabla \cdot \left(\left. \frac{\nabla \varphi}{|\nabla \varphi|} \right|_{\varphi=0} \right). \tag{11}$$

For computational efficiency, the adaptive mesh refinement (AMR) method was applied to enhance the computation speed (Fig. 4). The cells near the gas–liquid interface was refined in three layers with the smallest cell edge length of 0.0125 mm. The computational domain is $12 \times 12 \times 6 \, \text{mm}^3$. The wall is set as no slip stationary boundary. The velocity-inlet and the initial droplet loading are defined according to the needed conditions and other surfaces are set as pressure-outlet boundary. Considering pressure–velocity coupling, the PISO algorithm was applied. The body force weighted was adopted when calculating the pressure, second order upwind was for energy equation, and Geo-Reconstruct was adopted when tracking two-phase interface. The time step was determined by balancing the Courant number with the computational speed.

The simulation conditions of different droplet and moving film parameters were listed in Table I. Droplets Weber number We_d and Reynolds number of the moving film Re_f are calculated as the following equations:

$$We_d = \frac{\rho v_0^2 d_0}{\sigma}, \tag{12}$$

$$Re_f = \frac{\rho v_f h_f}{\mu}. \tag{13}$$

B. Validation of the numerical model

Successive droplets impacting on the inclined dry-wall and the vertical moving film were simulated and then, to further examine the
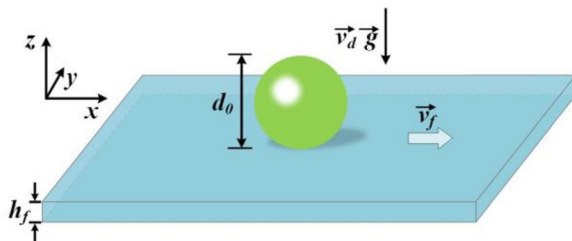

FIG. 4. Schematic of computational domain of spherical droplet impacting the moving film.

TABLE I. Simulation case no. and parameters.

Case no.	d_0 (mm)	v_0 (m/s)	h_f (mm)	v_f (m/s)	Re_f	We_d
1	2.0	3.0	0.295	0.966	281.161	246.387
2	2.0	3.37	0.295	0.966	281.161	310.911
3	2.0	3.37	0.295	0.5	145.528	310.911
4	2.0	3.0	0.295	0.5	145.528	246.387
5	2.0	2.8	0.295	0.5	145.528	214.631
6	2.0	2.0	0.2	1.5	295.990	109.505
7	2.0	3.0	0.2	1.5	295.990	246.387
8	2.42	2.446	0.315	0.688	213.823	198.187
9	2.0	2.5	0.295	0.5	145.528	171.102
10	2.0	2.1	0.295	0.5	145.528	120.730

developed simulation model, both compared with the corresponding experimental results as follows.

1. Validation of droplet train impacting on the inclined surface

Droplets impacting inclined wall is a common process which was reproduced accurately. To better reproduce the impacting process, a dynamic contact angle model[48] was implemented in the solver. Two sets of experiments were conducted under inclined angles of 30.9° and 59.9°, with other experimental parameters listed in Table II. The experimental results were validated through simulations, and the comparisons between the two are presented in Fig. 5. Droplet train impacting the inclined wall at 30.9°: (a)–(d) and (i)–(l) for experimental results and (e)–(h) and (m)–(p) for simulation results, respectively (Fig. 6). Upon impact, the droplets spread radially outwards under inertia after impacting the inclined wall. The propagation of the liquid is gradually asymmetric owing to the tangential velocity component $\vec{v_t}$ and tangential gravity component $\vec{g_t}$. The liquid elongation under the influence of gravity and the front-to-back asymmetry grow as time progresses. Liquid flowing downward along the tangential direction is affected by wall resistance and surface tension, thus stacking downstream while thinning upstream occurs.

Figure 7 shows the variation of the dimensionless spreading distance d_s^* (calculated as $d_s^* = d_s/d_0$) over time for both experimental and simulation results of droplet impact on inclined walls. It can be observed that the spreading velocity of the droplets is significantly faster when $\theta = 59.9°$. For 30.9° and 59.9°, the mean absolute errors (MAE) between the experimental and simulation results are 0.099 and 0.081, respectively, indicating a good agreement. MAE is calculated by the following equation:

TABLE II. Experimental parameters for droplet impact on inclined walls.

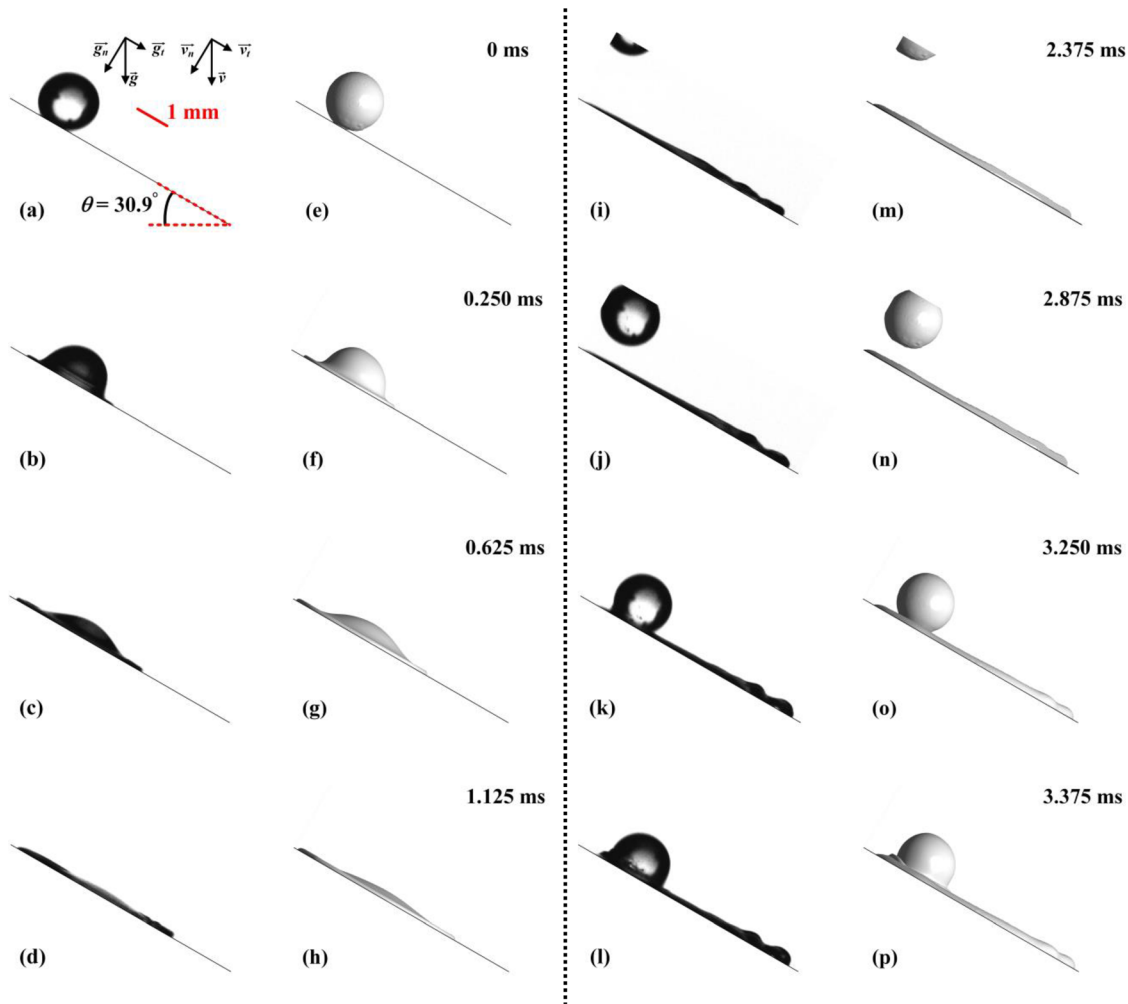| θ	d_0 (mm)	v_0 (m/s)	f (Hz)	We_d	Re_d
30.9°	1.802	2.545	320	159.76	4524.79
59.9°	1.981	2.824	364	216.25	5519.57

FIG. 5. Droplet train impacting the inclined wall at 30.9°: (a)–(d) and (i)–(l) for experimental results and (e)–(h) and (m)–(p) for simulation results.

$$\text{MAE} = \frac{1}{n} \sum_{i=1}^{n} |y_i - \hat{y}_i|, \qquad (14)$$

where y_i, $\hat{y}_i$, and n denoted the numerical and experimental results and the amount of the data, respectively.

2. Validation of droplet impacting on the flow film

The simulation model was validated as shown in Fig. 8 ($We_d = 198.187$ and $Re_f = 213.823$). The crowns appeared after the impact showing a significant asymmetry of being higher upstream than downstream. In addition, the liquid sheet upstream tended to extend horizontally, which can also be seen from the curvature. Since the film flow affects the crown development, the liquid sheet downstream of the crown tilted toward upstream in the pre-development stage as follows:

$$t^* = \frac{t * v_0}{d_0}. \qquad (15)$$

When the dimensionless time t^*, defined as Eq. (15), equals 0.758, fingerlike protrusions appeared on the crown edge upstream. As it continues to develop, the protrusions will gradually escape from the control of surface tension and break into secondary droplets. The quantitative comparison of R_u and R_d were shown as Fig. 9. The MAE of dimensionless spreading distance R_u^* and R_u^* are 0.069 and 0.015, respectively, which shows a great agreement between the experiment and simulation.

IV. SINGLE DROPLET IMPACT ON THE MOVING FILM
A. Evolution and analysis of impact

The major difference in crown formation is the occurrence and intensity of splashing and secondary droplets. As the liquid film flows downstream, an upstream shear stress develops between the film and the droplet, leading to the crown inclined to upstream. Since the variable droplet and film parameters, the discussion is focus on the influence of both We_d and Re_f on the crown formation.
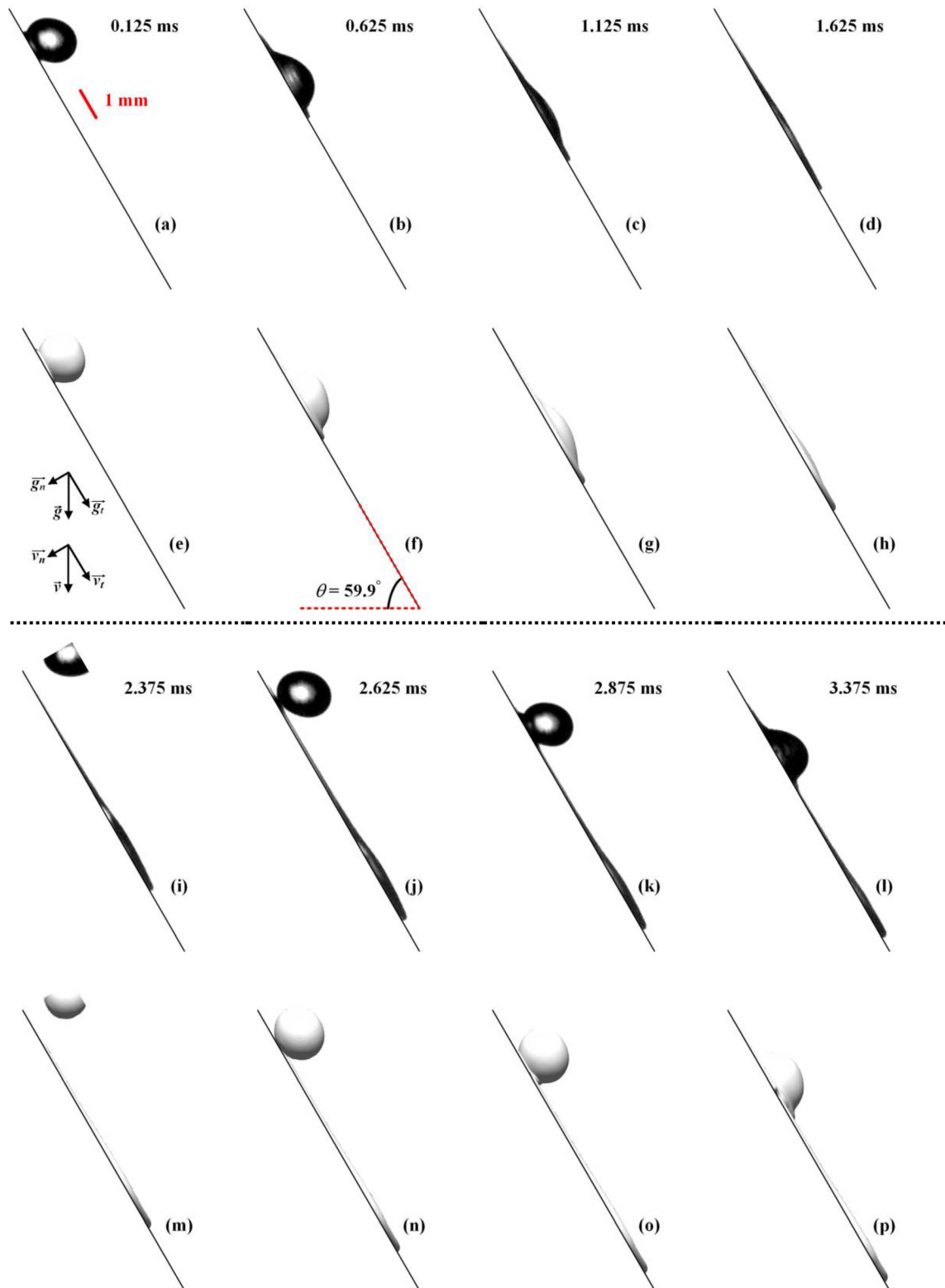
06 March 2025 14:54:52

FIG. 6. Droplet train impacting the inclined wall at 59.9°: (a)–(d) and (i)–(l) for experimental results and (e)–(h) and (m)–(p) for simulation results.
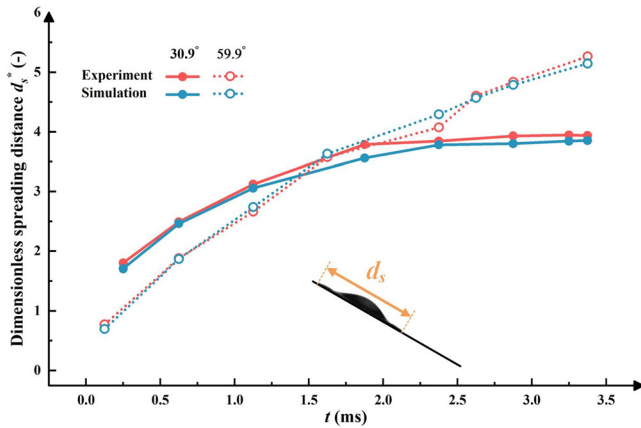
FIG. 7. Quantitative comparison of dimensionless spreading distance for the experiment and simulation.

FIG. 9. Quantitative comparisons of dimensionless spreading distance with dimensionless time for experimental and numerical results.

Only considering case 3, secondary droplets appear earlier due to the film velocity v_f. When Re_f is fixed, the influence of We_d on the occurrence and the morphological evolution of the crown is illustrated in Fig. 9. For case 5 ($We_d = 214.631$), the crown downstream is not fully formed until $t = 0.4$ ms, and before that, it is suppressed and no liquid sheet has been produced. In case 3 ($We_d = 310.911$), the liquid sheet upstream and downstream are formed at 0.2 ms, and then
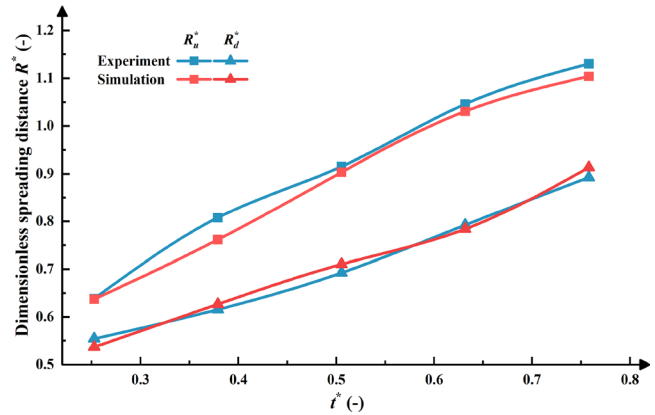
gradually develop with time, becoming taller and larger. Meanwhile, the crown is more prone to breaking up when We_d is larger. In Figs. 10(c) and 10(h), secondary droplets appear when $We_d = 310.911$ but not when $We_d = 214.631$. Additionally, with a larger We_d, the asymmetry of the crown height is weakened. With larger initial droplet kinetic energy, the liquid sheets are generated with the larger velocities and are more likely to break.
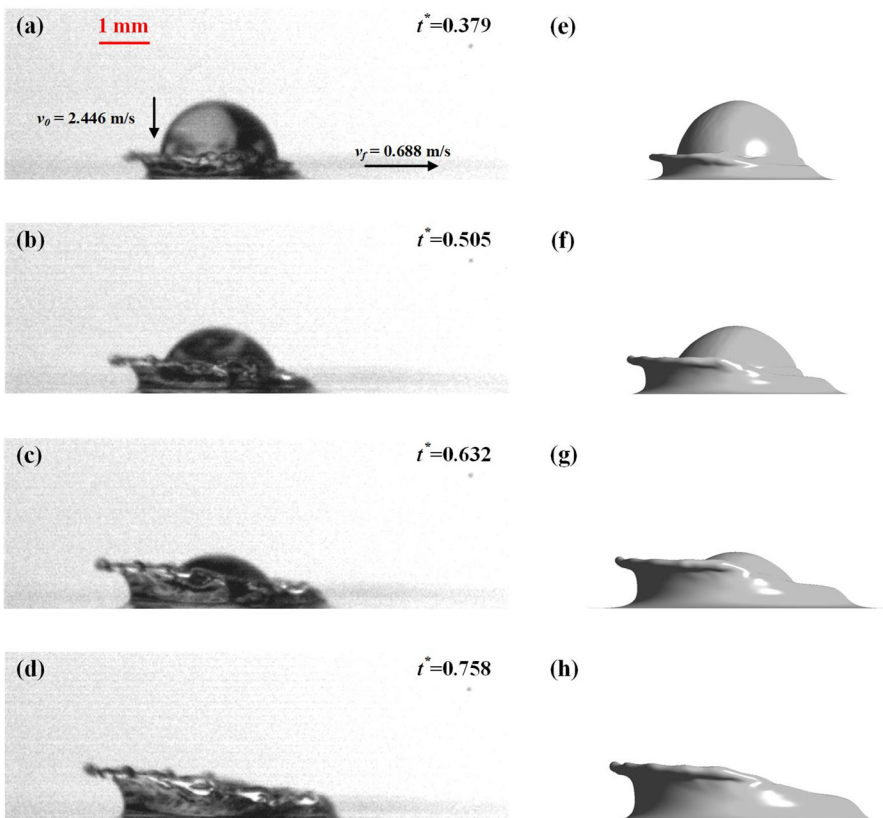

FIG. 8. Morphology for experiment and simulation of case 8: (a)–(d) for experimental results and (e)–(h) for simulation results.
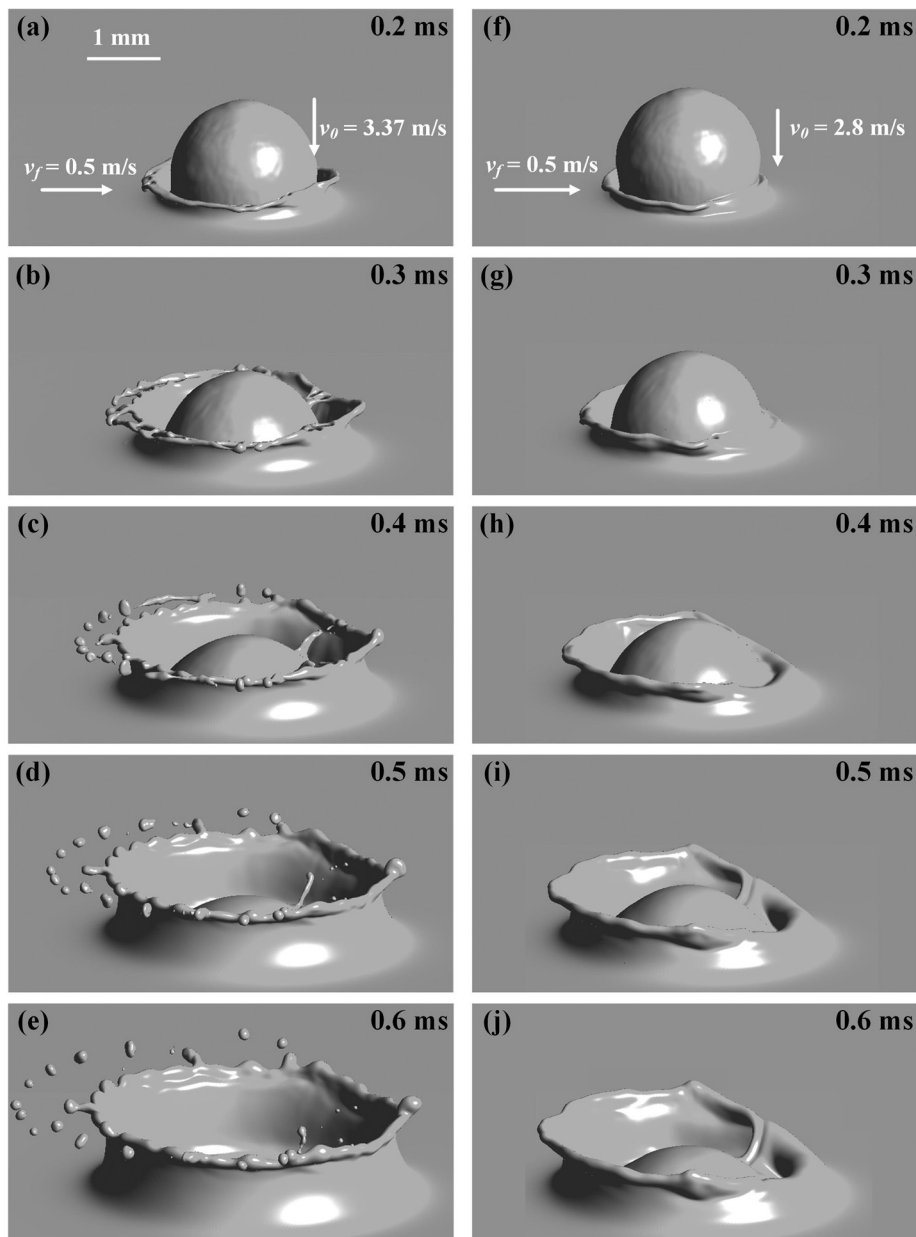
06 March 2025 14:54:52

FIG. 10. Evolution of the droplet morphology when different We_d ($Re_f = 145.528$): (a)–(e) for case 3 at $We_d = 310.911$ and (f)–(j) for case 5 at $We_d = 214.631$.

When We_d is fixed, the larger Re_f is, the larger the trailing force the liquid sheet downstream is suffered with larger v_f and the front-to-back spreading distance between the edge of the crown upstream and downstream is during the same time. Additionally, with the larger Re_f, the liquid sheet downstream is more suppressed. When $t = 0.2$ ms, the liquid sheet downstream of case 4 has already appeared, while when $t = 0.4$ ms, the liquid sheet downstream of case 1 is only gradually molded even though it is still inhibited. Regarding the secondary droplet generation, the liquid sheet is more prone to breaking up into small secondary droplets with larger Re_f (Fig. 11). When $t = 0.6$ ms, secondary droplets have already appeared in case 1, but the fingerlike protrusions has just appeared on the liquid sheet upstream in case 4.

Quantitative evolution of R_u^* and R_d^* with fixed We_d are shown in Fig. 12. R_u^* and R_d^* are overall positively correlated with Re_f. In Fig. 12(a), where Re_f is close, R_u^* is also relatively close. Although the evolution of R_u^* over time for cases 1 and 7 is quite similar, the time-dependent evolution of R_d^* shows significant differences, which indirectly reflects the asymmetry in the development of the crown. In Fig. 12(b), the change in R_d^* is more significant as Re_f grows because the crown downstream is more affected by the trailing force of the film. Meanwhile, with larger Re_f, the liquid sheet of the crown downstream appears relatively later. For example, when $Re_f = 295.990$ in case 7, the jet downstream appears until $t^* = 0.36$. It also substantiates that the crown downstream is more suppressed with larger Re_f.
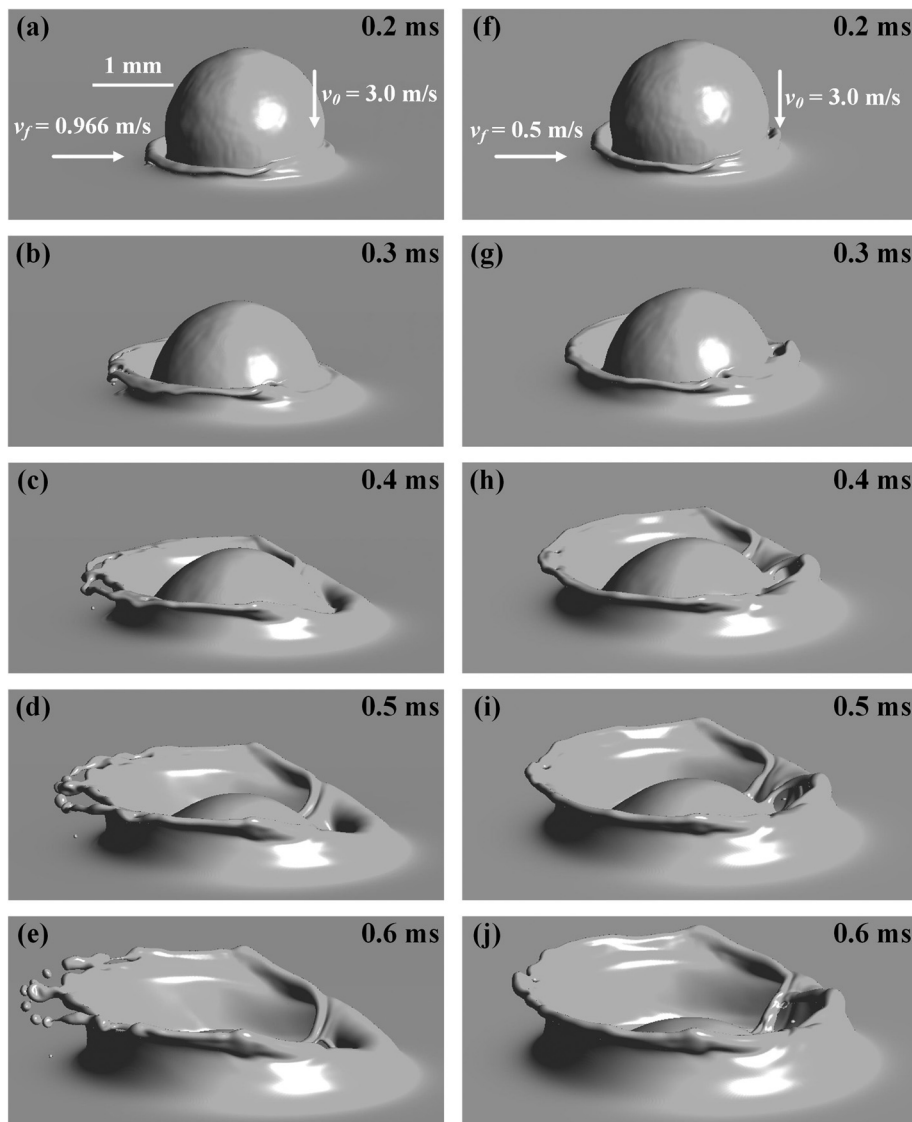
FIG. 11. Evolution of the droplet morphology when different Re_f ($We_d = 246.387$): (a)–(e) for case 1 at $Re_f = 281.161$ and (f)–(j) for case 4 at $Re_f = 145.528$.

In Fig. 13, both R_u^* and R_d^* clearly increase with We_d under the condition of $Re_f = 145.528$. This indicates that as the droplet velocity increases, the initial kinetic energy of the droplet increases, thereby providing more energy to the crown, allowing it to propagate further. A sudden turning point occurs when $We_d = 310.911$ in Fig. 13(a), which is attributed to crown breakup and the formation of secondary droplets upstream, leading to a sudden decrease in R_u^* from 1.090 to 1.047. In Fig. 13(b), R_d^* is generally positively correlated with We_d. The values of R_u^* for the five cases reach 1.059, 1.101, 1.173, 1.212, and 1.267, respectively, as We_d increases when $t^* = 1$. Both R_u^* and R_d^* exhibit a power-law evolution with respect to the dimensionless time, similar to the conclusion in Refs. 41 and , and the fitting curve is also shown in Fig. 13. However, the exponents for the upstream and downstream differ. The exponent for the upstream is approximately 0.435, while for the downstream it is about 0.543. The difference in exponents

suggests that the evolution of the crown in the upstream and downstream over time is asymmetrical.

We_d also influences the development of the crown. A further analysis of the results in Fig. 13 reveals that the spreading behavior of the crown over time is positively correlated with We_d raised to the power of 0.2, and this relationship holds for both the upstream and downstream. As shown in Fig. 14, in the upstream and downstream, the relationships $R_u^*/We_d^{0.2} \propto t^{*0.435}$ and $R_d^*/We_d^{0.2} \propto t^{*0.543}$, respectively, exhibit approximate linearity. Reference 43 mentions that the dimensionless maximum spreading factor after droplet impact is positively correlated with $We_d^{0.2}$ in the low We_d, which is consistent with our findings. This further supports the conclusion that, under the same Re_f, the evolution of droplets after impact with a flowing liquid film is significantly influenced by t^* and We_d.
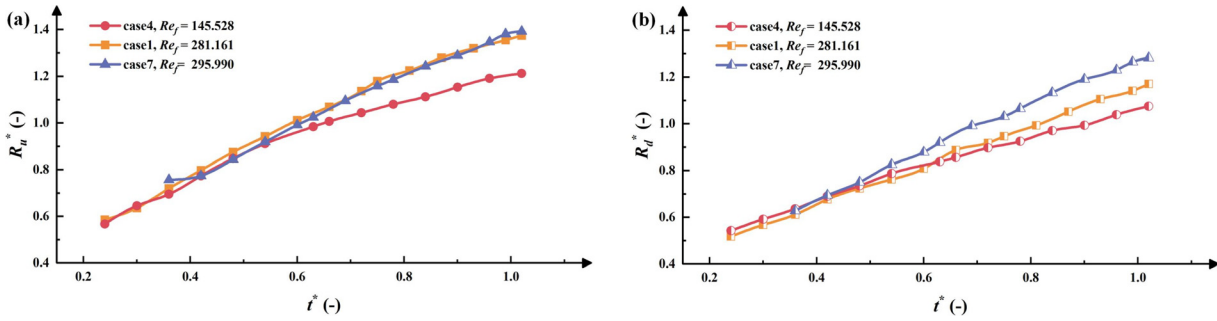
FIG. 12. Dimensionless spreading distance upstream and downstream evolution with $t*$ when $We_d = 246.387$: (a) R_u^* and (b) R_d^*.
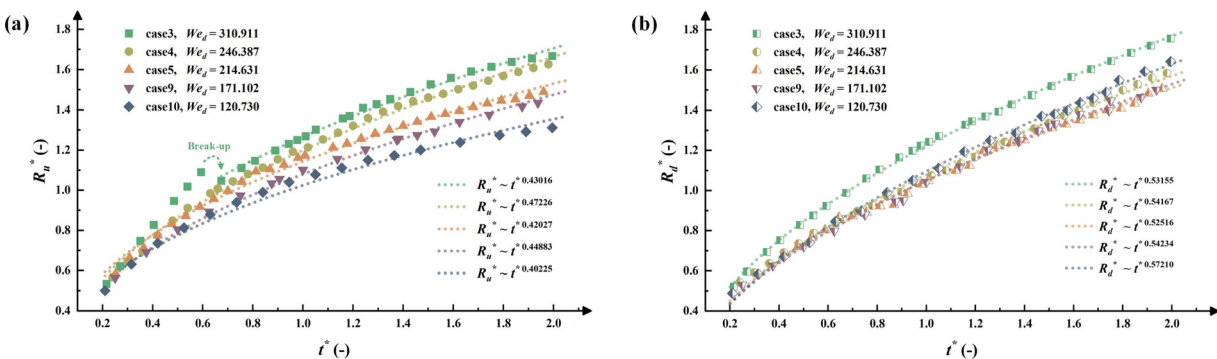

FIG. 13. Dimensionless spreading distance upstream and downstream evolution with $t*$ when $Re_f = 145.528$: (a) R_u^* and (b) R_d^*.
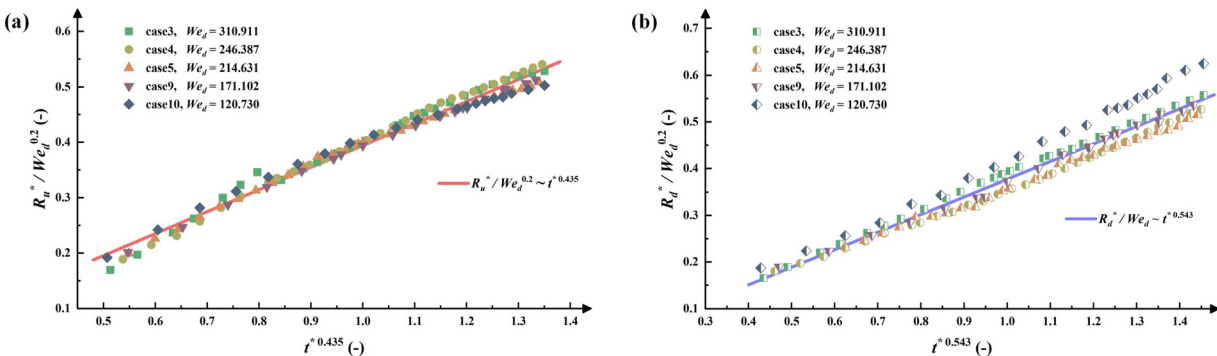

FIG. 14. Dimensionless spreading distance upstream and downstream evolution with $t*$ and We_d when $Re_f = 246.387$: (a) $R_u^*/We_d^{0.2} \propto t^{*0.435}$ and (b) $R_d^*/We_d^{0.2} \propto t^{*0.543}$.

The gas–liquid interface profiles and velocity vector fields on ZOX cross section for case 3 are plotted in Fig. 15. Around the impact position, the liquid inside the droplet turns violently from downward to horizontal. A velocity discontinuity occurs when the fast-moving liquid meets the film resulting in the liquid move upward into the jets. When $t = 0.098$ ms, there is a very large velocity of 8.07 m/s at the neck, which contributes to the extension upward and outward into the crown under the inertial force. During the subsequent evolution, a clockwise velocity vortex around the left jet, while there is a large counterclockwise vortex is around the right jet. Once the crown expands outward, the difference

in the moving velocity of the crown root upstream and downstream can predict the next extension direction in Fig. 15(b). When $t = 0.592$ ms, the velocity of the crown root downstream reaches 3.79 m/s, while that upstream is only 2.83 m/s. This is because the jet upstream moves in the direction opposite to the film flow thus being resisted, while the jet downstream moves in the same direction, thus being pushed forward. Especially, the velocity in the connection region between the fingerlike protrusions and the liquid sheet before the formation of the secondary droplets is large. For example, the velocity in the connection region of the jet upstream in Fig. 15(d) reaches 5.03 m/s.
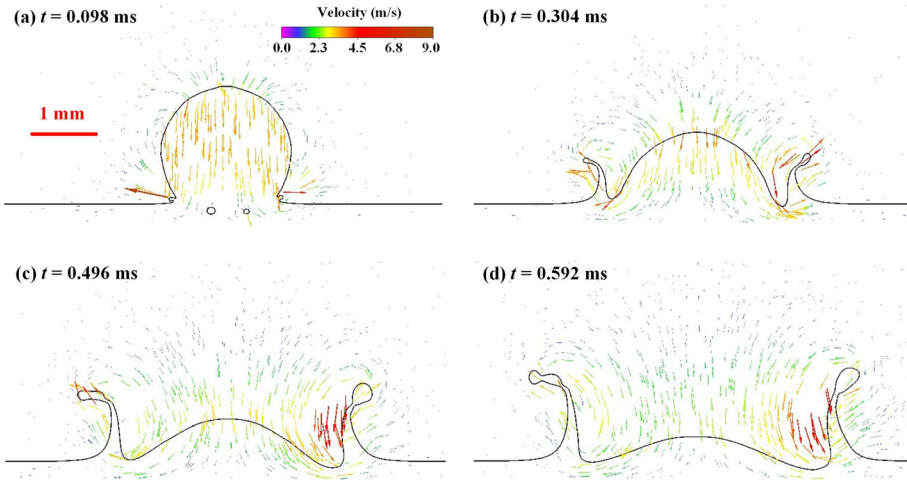
FIG. 15. Velocity vector of case 3 at different time points: (a) $t = 0.098$ ms; (b) $t = 0.304$ ms; (c) $t = 0.496$ ms; and (d) $t = 0.592$ ms.

B. Energy evolution during the impact

During the impact process, the formation of the crown or secondary droplets appear is heavily influenced by the energy imparted to the crown from the impact. The energy in the impact process comes from droplet's kinetic energy, potential energy, and surface energy. Thus, it is necessary to analyze how the initial energy carried by the droplet evolves and dissipates throughout the impact process.

E_s refers to the surface energy at the gas-liquid interface, defined as surface tension σ times gas–liquid interfacial area A_{G-L}, as shown in Eq. (16). In addition, A_{G-L} was obtained by summing the gas–liquid interfacial area of each cell A_i on the interface

$$E_s = \sigma A_{G-L} = \sigma \sum_{i=0}^{n} |A_i|. \quad (16)$$

The total kinetic energy E_k was calculated as the sum of each cell's kinetic energy E_{ki} as the following equation:

$$E_k = \sum_{i=0}^{n} E_{ki} = \sum_{i=0}^{n} \frac{1}{2} m_i v_i^2. \quad (17)$$

The potential energy E_p was obtained from the following equation:

$$E_p = m_{total} g z_c = g \sum_{i=0}^{n} m_i \frac{\sum_{i=0}^{n} m_i z_i}{\sum_{i=0}^{n} m_i} = g \sum_{i=0}^{n} m_i z_i, \quad (18)$$

where z_c was the center of gravity of these cells and m_i was the mass of each cell i. E_{total} was defined as the sum of above energies, and the initial energy of the droplet was composed as

$$E_0 = E_{total} + W = E_s + E_k + E_p + W, \quad (19)$$

where W is the energy dissipation. The changes in E_{total} during the impact process in two different cases are demonstrated in Fig. 16. Because of the formatted crown, the surface energy E_s declines first followed by a gradual recovery, reaching a minimum value of 6.860×10^{-7} J at $t = 0.127$ ms in Fig. 16(a). In contrast with Fig. 16(b), E_s continues to decrease in the early stage due to the absence of a rapidly elevating and enlarging crown and only shows a small rebound after $t = 0.36$ ms. This also reflects that the formation and development of the crown will greatly contribute to the increase in A_{G-L}. During the cooling process, A_{G-L} greatly affects the heat transfer so considering the change of E_s during the impact is needed. The kinetic energy E_k consumption accounts for a large proportion of the change
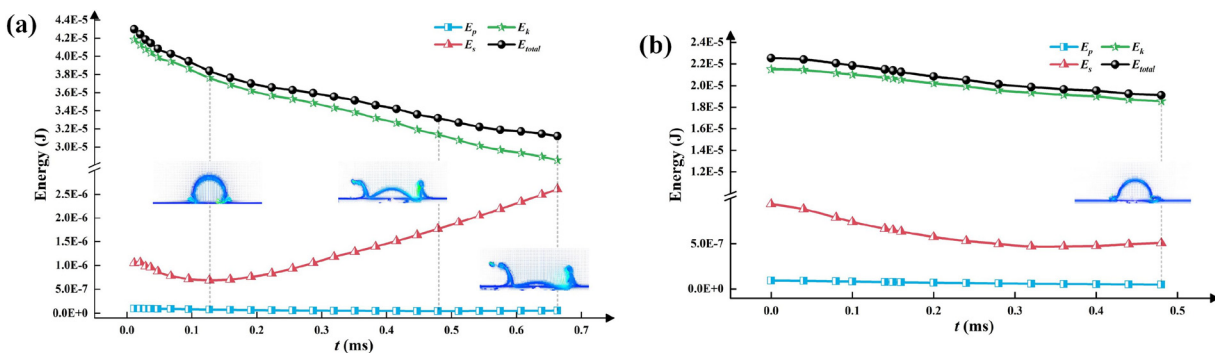

FIG. 16. Energy evolution during the impact with corresponding velocity vector: (a) case 2 ($Re_f = 281.161$ and $We_d = 310.911$) and (b) case 6 ($Re_f = 295.990$ and $We_d = 109.505$).
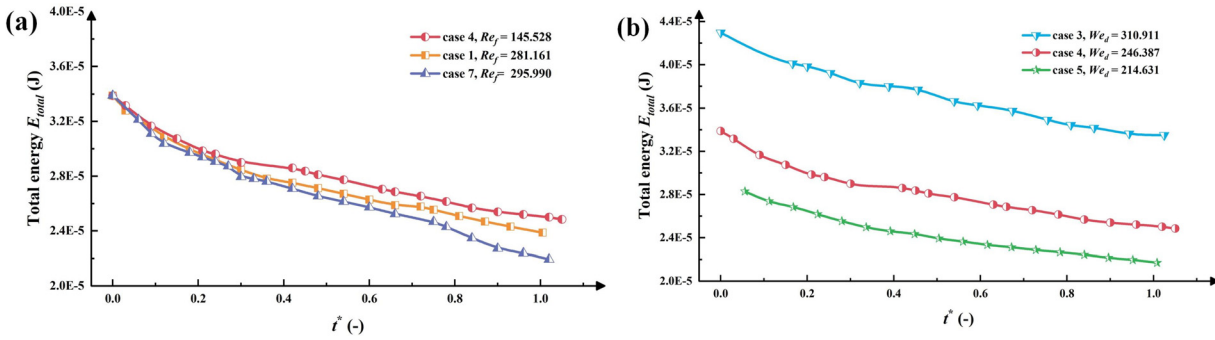
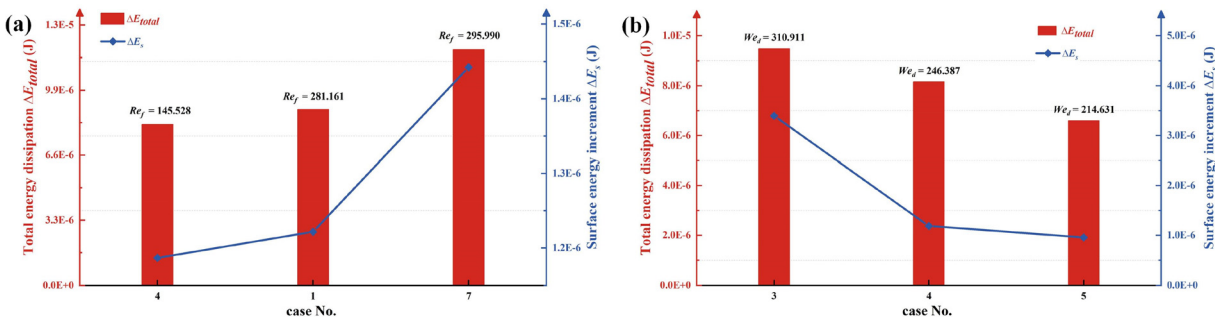**FIG. 17.** Total energy evolution with dimensionless time when (a) $We_d = 145.528$ and (b) $Re_f = 246.387$.

FIG. 18. Energy consumption when $t* = 1$: (a) cases 1, 4, 7, the same We_d (145.528) and (b) cases 3–5, the same Re_f (246.387).

of E_{total}, it affects the trend E_{total} more. For case 2, during $t = 0.6631$ ms, the decrease in E_k is 1.3301×10^{-5} J, while ΔE_{total} is 1.1786×10^{-5} J. This reflects that although ΔE_k determines the change of E_{total}, the increase in E_s also plays a role. And it is obvious that because We_d is greater for case 6, the energy dissipation W is significantly greater, with the larger Re_f in case 6 which reveals the greater influence of We_d on energy dissipation.

The variation of E_{total} for the same We_d and Re_f is presented, respectively, in Figs. 17(a) and 17(b) to compare the effect of Re_f and We_d on energy dissipation more clearly. When $We_d = 145.528$, E_{total} decreases more from the same initial value as Re_f increases. When We_d are the same in Fig. 17(a), initial E_{total} of the three cases is 3.389×10^{-5} J. By $t* = 1.02$, ΔE_{total} of case 7, which has a larger Re_f, is 2.193×10^{-5} J, which is 0.257×10^{-5} J less than the ΔE_{total} of case 4, which is 2.450×10^{-5} J. When $Re_f = 246.387$, as We_d increases, with the larger initial droplet energy, E_{total} decreases in a very similar trend.

To further explore the energy change under different conditions, the energy dissipation W, i.e., ΔE_{total}, and the increment of surface energy ΔE_s within $t* = 1$ are presented in Fig. 18. In Fig. 18(a), when $We_d = 145.528$, ΔE_{total} increases as Re_f increases. Comparing cases 4 and 7, it is observed that ΔE_s becomes larger by 0.256×10^{-6} J, but ΔE_{total} increases by 3.80×10^{-6} J. This demonstrates that although ΔE_s increases, ΔE_{total} still continues to follow the trend of increasing with Re_f due to the gradual increase in the dissipation of E_k. In Fig. 18(b), when $Re_f = 246.387$, ΔE_{total} is positively related to We_d.

Comparing cases 3 and 5, it can be found that ΔE_s is only reduced by 2.438×10^{-6} J, while ΔE_{total} reduced by 2.88×10^{-6} J. Although ΔE_s decreases, ΔE_{total} still maintains the tendency to become larger with We_d because the dissipation of kinetic energy becomes smaller.

V. SUCCESSIVE DROPLET IMPACT ON MOVING LIQUID FILM

Even though single droplet impacting the liquid are widely investigated, successive droplets impacting the moving film are more common in reality. The parameters of simulations for successive droplets impact at different conditions were listed in Table III.

As shown in Fig. 19, the fingerlike protrusions on the liquid crown are tilted upstream relative to the crown root due to the flow of the film. A high-velocity connection region forms between the protrusions and the liquid sheet of the crown. Splashing secondary droplets are generated as the protrusions struggle to overcome surface tension after progressing upward and outward. The dimensionless time

TABLE III. Parameters when successive droplets impacting on the moving film.

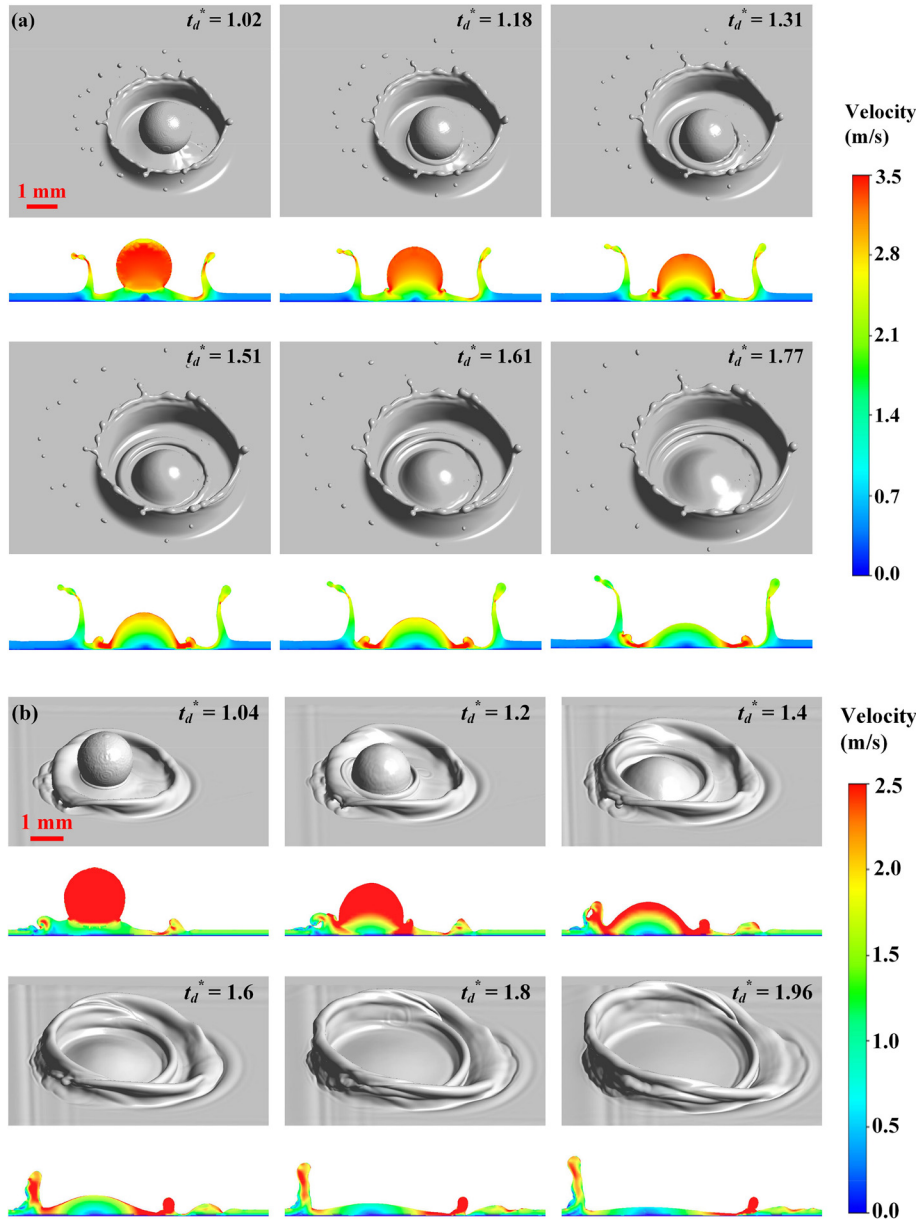| No.	f (Hz)	D_0 (mm)	v_0 (m/s)	h_f (mm)	v_f (m/s)	Re_f	We_d
3	1600	2.0	3.37	0.295	0.5	145.528	310.911
6	1000	2.0	2.0	0.2	1.5	295.990	109.505

FIG. 19. Evolution of the morphology of the successive droplets impacting flow film and the velocity field of the ZOX section at $Y = 0.6$ mm: (a) case 3, $Re_f = 281.161$, $We_d = 310.911$ and (b) case 6, $Re_f = 295.990$, $We_d = 109.505$.

$t_d^* = tf$ is defined to account for the successive impact of droplets on the moving film. When $t_d^* = 1.02$, the velocity is higher at necks where the liquid crown begins to forming, which cause a further expansion of the crown height and spreading distance. When $t_d^* > 1$, the subsequent droplet starts to impact the film inside the outer crown caused by the impact of the former droplet. The droplet with the higher velocity gradually falls down, bringing a partial energy transferred to the new neck. This can also be seen in the velocity field as shown in Fig. 19.

As the film flows downstream, the downstream liquid sheets of both the inner and outer crowns move in the same direction, and they do not coalesce for a brief period. However, since the downstream liquid sheet of the inner crown encounters a thinner film during

spreading and experiences less resistance, the inner crown advances downstream at a faster rate. When $t_d^* = 1.77$, the upstream liquid sheets of the inner and outer liquid crown are almost merged, while when $t_d^* = 1.97$ and $R_u^* = 1.689$, the upstream liquid sheets of the inner and outer liquid crowns are completely converged as shown in Fig. 20(a). Due to the low frequency of case 6, the time interval between the two droplets is larger comparing with case 2. As a result, the subsequent droplet impacts closer to the liquid sheet upstream of the outer crown, causing the liquid sheets upstream of the inner and outer crowns to merge earlier. When $t_d^* = 1.2$, the upstream liquid sheets of the inner and outer liquid crowns are almost merged. When $t_d^* = 1.4$ and $R_u^* = 0.881$, the upstream liquid sheets of the inner and
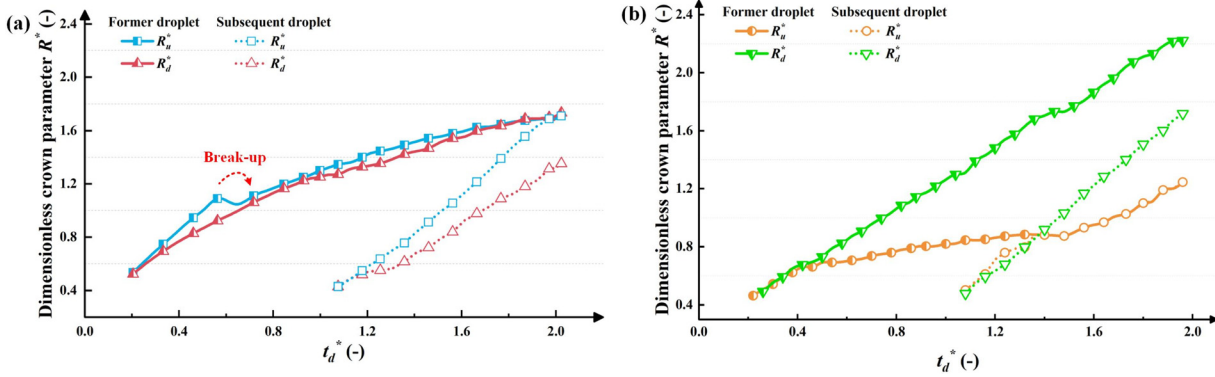
FIG. 20. Dimensionless crown spreading distance R_u^* and R_d^* of successive droplet impacting the moving film: (a) case 2, $Re_f = 281.161$, $We_d = 310.911$ and (b) case 6, $Re_f = 295.990$, $We_d = 109.505$.

outer liquid crowns are completely converged as shown in Fig. 20(b). In contrast to Fig. 20(a), for case 6, R_d^* is significantly larger than R_u^* and the crown asymmetry is more pronounced due to the larger Re_f. This also validates the conclusions of Sec. IV A.

VI. CONCLUSIONS

A three-dimensional model based on VOF model and AMR was developed to simulate the droplets impacting the moving film. The dimensionless number We_d was changed by varying droplet diameter and velocity, and the dimensionless number Re_f was changed by varying the film velocity and thickness. The morphology and energy evolution were studied according to them. Following conclusions were summarized.

(1) Due to the horizontal velocity difference of the film and droplets, crown asymmetry appears. With larger We_d, the crown spreads higher and larger, becomes more likely to break up, but exhibits reduced asymmetry. With larger Re_f, the front-to-back spreading distance is greater, and the crown is more likely to break up. When We_d is less and Re_f is larger, the crown downstream is more suppressed; thus, the crown asymmetry is more obvious.

(2) When $Re_f = 145.528$, the dimensionless upstream and downstream radii of the liquid crown, R_u^* and R_d^*, approximately follow a power–law relationship with dimensionless time $t*$, and are positively correlated with $We_d^{0.2}$. The evolution of the upstream and downstream radii can be approximately represented as $R_u^*/We_d^{0.2} \propto t^{*0.435}$ and $R_d^*/We_d^{0.2} \propto t^{*0.543}$.

(3) The kinetic energy dissipation is the major part of total energy dissipation. Higher We_d and Re_f lead to greater energy dissipation during the same period of dimensionless time. The surface energy E_s increases due to the increased gas–liquid interface from the crown, and the increment of E_s is positively correlated with We_d and Re_f.

(4) Crown moves upward and outward due to the pre-existing higher velocity of roots. Fingerlike protrusions at the rim of the crown struggle out of the surface tension and become secondary droplets.

(5) When successive droplets impacting the moving film, the liquid sheet upstream of the inner and outer crowns are more likely to merge. The downstream of the inner crown is less resisted by the moving film and advances at a greater speed although it keeps a distance from the downstream of the outer crown.

AUTHOR DECLARATIONS
Conflict of Interest

The authors have no conflicts to disclose.

Author Contributions

Hongbing Ding: Conceptualization (equal); Formal analysis (equal); Funding acquisition (equal); Methodology (equal); Writing – original draft (equal). **Xutian Chai:** Formal analysis (equal); Methodology (equal); Visualization (equal); Writing – review & editing (equal). **Xinyu Song:** Formal analysis (equal); Methodology (equal); Visualization (equal); Writing – review & editing (equal). **Yan Yang:** Conceptualization (equal); Formal analysis (equal); Methodology (equal); Supervision (equal); Writing – review & editing (equal). **Chuang Wen:** Conceptualization (equal); Formal analysis (equal); Investigation (equal); Methodology (equal); Supervision (equal); Writing – review & editing (equal).

DATA AVAILABILITY

The data that support the findings of this study are available from the corresponding authors upon reasonable request.

REFERENCES

[1]Z. Hu, F. Chu, H. Shan et al., "Understanding and utilizing droplet impact on superhydrophobic surfaces: Phenomena, mechanisms, regulations, applications, and beyond," Adv. Mater. **36**(11), 2310177 (2024).

[2]B. Chen, Y. Zhang, Z. Dai et al., "Experimental research on the dynamics of a train of droplets impacting, from droplets to liquid film, continuity and inheritance," Energy **256**, 124670 (2022).

[3]J. Kim and J. Kang, "AI based temperature reduction effect model of fog cooling for human thermal comfort: Climate adaptation technology," Sustainable Cities Soc. **95**, 104574 (2023).

[4]C. D. Modak, A. Kumar, A. Tripathy et al., "Drop impact printing," Nat. Commun. **11**(1), 4327 (2020).

[5]H. Ding, J. Zhao, Z. Zhang et al., "A numerical study on the interaction of droplet collisions and air flow impact in cross-impinging spray," Energy **277**, 127688 (2023).

[6]D. Zang, S. Tarafdar, Y. Y. Tarasevich et al., "Evaporation of a Droplet: From physics to applications," Phys. Rep. **804**, 1–56 (2019).

[7]M. Rein, "Phenomena of liquid drop impact on solid and liquid surfaces," Fluid Dyn. Res. **12**(2), 61–93 (1993).

[8]P. Xie, X. Lu, X. Yang et al., "Characteristics of liquid flow in a rotating packed bed for CO_2 capture: A CFD analysis," Chem. Eng. Sci. **172**, 216–229 (2017).

[9]Z. Zhang, H. Liu, F. Zhang et al., "Numerical study of spray micro-droplet impinging on dry/wet wall," Appl. Therm. Eng. **95**, 1–9 (2016).

[10]R. Cimpeanu and D. T. Papageorgiou, "Three-dimensional high speed drop impact onto solid surfaces at arbitrary angles," Int. J. Multiphase Flow **107**, 192–207 (2018).

[11]M. A. Mazloomi, S. S. Chikatamarla, and I. V. Karlin, "Entropic lattice Boltzmann method for multiphase flows," Phys. Rev. Lett. **114**(17), 174502 (2015).

[12]M. Sussman and E. G. Puckett, "A coupled level set and volume-of-fluid method for computing 3D and axisymmetric incompressible two-phase flows," J. Comput. Phys. **162**, 301–337 (2000).

[13]D. Khojasteh, M. Kazerooni, S. Salarian et al., "Droplet impact on superhydrophobic surfaces: A review of recent developments," J. Ind. Eng. Chem. **42**, 1–14 (2016).

[14]C. Josserand and S. T. Thoroddsen, "Drop impact on a solid surface," Annu. Rev. Fluid Mech. **48**, 365–391 (2016).

[15]S. Schubert, J. Steigerwald, A. K. Geppert et al., "Micro-PIV study on the influence of viscosity on the dynamics of droplet impact onto a thin film," Exp. Fluids **65**, 69 (2024).

[16]B. Chen, R. Tian, and F. Mao, "Analysis of special phenomena of droplet impact on horizontal liquid film at low velocity," Ann. Nucl. Energy **136**, 107038 (2020).

[17]S. Ding, Z. Hu, L. Dai, X. Zhang, and X. Wu, "Droplet impact dynamics on single-pillar superhydrophobic surfaces," Phys. Fluids **33**, 102108 (2021).

[18]Š. Šikalo, H. D. Wilhelm, I. V. Roisman et al., "Dynamic contact angle of spreading droplets: Experiments and simulations," Phys. Fluids **17**(6), 062103 (2005).

[19]H. Chu, X. Yu, H. Jiang et al., "Progress in enhanced pool boiling heat transfer on macro- and micro-structured surfaces," Int. J. Heat Mass Transfer **200**, 123530 (2023).

[20]A. M. Worthington, "The splash of a drop and allied phenomena," Sci. Am. **40**, 16402–16404 (1895).

[21]R. L. Vander Wal, G. M. Berger, and S. D. Mozes, "Droplets splashing upon films of the same fluid of various depths," Exp. Fluids **40**(1), 33–52 (2006).

[22]G. Liang, Y. Guo, S. Shen et al., "Crown behavior and bubble entrainment during a drop impact on a liquid film," Theor. Comput. Fluid Dyn. **28**(2), 159–170 (2014).

[23]S. Bakshi, I. V. Roisman, and C. Tropea, "Investigations on the impact of a drop onto a small spherical target," Phys. Fluids **19**(3), 32102 (2007).

[24]J. P. Muthusamy, T. Zhang, J. L. Alvarado et al., "Hydrodynamic and heat transfer characteristics of droplet train spreading-splashing transition on heated surface," Int. J. Heat Mass Transfer **164**, 120500 (2021).

[25]J. He, H. Yuan, X. He et al., "Droplet impact on a moving thin film with pseudopotential lattice Boltzmann method," Math. Probl. Eng. **2020**, 1–15.

[26]J. L. Stober, M. Santini, and K. Schulte, "Influence of Weber number on crown morphology during an oblique droplet impact on a thin wall film," Fluids **8**(11), 301 (2023).

[27]Z. Chen, C. Shu, Y. Wang et al., "Oblique drop impact on thin film: Splashing dynamics at moderate impingement angles," Phys. Fluids **32**, 033303 (2020).

[28]M. Cheng and J. Lou, "A numerical study on splash of oblique drop impact on wet walls," Comput. Fluids **115**, 11–24 (2015).

[29]T. Okawa, T. Shiraishi, and T. Mori, "Effect of impingement angle on the outcome of single water drop impact onto a plane water surface," Exp. Fluids **44**(2), 331–339 (2008).

[30]B. Ray, G. Biswas, and A. Sharma, "Oblique drop impact on deep and shallow liquid," Commun. Comput. Phys. **11**(4), 1386–1396 (2012).

[31]Y. Cao, J. Wang, and C. Zhu, "Numerical simulation of microscale oblique droplet impact on liquid film," Aerospace **10**(2), 119 (2023).

[32]D. Li, Y. Shang, X. Wang et al., "Dynamic behavior of droplet impacting on a moving surface," Exp. Therm. Fluid Sci. **153**, 111126 (2024).

[33]C. Ming and L. Jing, "Lattice Boltzmann simulation of a drop impact on a moving wall with a liquid film," Comput. Math. Appl. **67**(2), 307–317 (2014).

[34]G. Liang, L. Li, L. Chen et al., "Impact of droplet on flowing liquid film: Experimental and numerical determinations," Int. Commun. Heat Mass Transfer **126**, 105459 (2021).

[35]X. Gao and R. Li, "Impact of a single drop on a flowing liquid film," Phys. Rev. E **92**(5), 053005 (2015).

[36]K. Zhao, Y. Wang, Y. Ding et al., "Numerical and theoretical study on the spreading characteristics of droplet impact on a horizontal flowing liquid film," Colloids Surf., A **616**, 126338 (2021).

[37]Y. Wu, B. Kong, B. Tong et al., "Oblique impact of droplet on a moving film in spray cooling," Eur. J. Mech. B **100**, 21–36 (2023).

[38]Z. Che, A. Deygas, and O. K. Matar, "Impact of droplets on inclined flowing liquid films," Phys. Rev. E **92**(2), 023032 (2015).

[39]L. Shan, Y. Song, S. Zhou et al., "Experimental and numerical study of droplet impact on radially flowing liquid film," Ind. Eng. Chem. Res. **62**(4), 2008–2020 (2023).

[40]G. Liang, Y. Chen, L. Chen et al., "Maximum spreading for liquid drop impacting on solid surface," Ind. Eng. Chem. Res. **58**(23), 10053–10063 (2019).

[41]R. Rioboo, M. Marengo, and C. Tropea, "Time evolution of liquid drop impact onto solid, dry surfaces," Exp. Fluids **33**(1), 112–124 (2002).

[42]T. Khan, Z. Jin, and Z. Yang, "Impact dynamics of non-spherical droplets on a thin water film," Phys. Fluids **36**(3), 032130 (2024).

[43]Y. F. Wang, Y. B. Wang, X. He et al., "Scaling laws of the maximum spreading factor for impact of nanodroplets on solid surfaces," J. Fluid Mech. **937**, A12 (2022).

[44]S. K. Alghoul, C. N. Eastwick, and D. B. Hann, "Normal droplet impact on horizontal moving films: An investigation of impact behaviour and regimes," Exp. Fluids **50**(5), 1305–1316 (2011).

[45]C. W. Hirt and B. D. Nichols, "Volume of fluid (VOF) method for the dynamics of free boundaries," J. Comput. Phys. **39**(1), 201–225 (1981).

[46]J. U. Brackbill, D. B. Kothe, and C. Zemach, "A continuum method for modeling surface tension," J. Comput. Phys. **100**(2), 335–354 (1992).

[47]Ansys Fluent, *18.1 Theory Guide* (Ansys Inc., 2017), pp. 510–543.

[48]P. Xie, H. Ding, D. B. Ingham et al., "Analysis and prediction of the gas-liquid interfacial area for droplets impact on solid surfaces," Appl. Therm. Eng. **178**, 115583 (2020).

06 March 2025 14:54:52